# Azimuthal PP and PS seismic amplitude variation with angle inversion for orthogonal fracture weaknesses

Huaizhen Chen[*] and Kristopher A. Innanen

## ABSTRACT

Characterization of fracture connectivity is an important task in detection of fractures in hydrocarbon reservoirs. The current reflection coefficients are mainly derived under the assumption of horizontal or tilted transversely isotropic (HTI or TTI) media for a rock containing a single set of aligned fractures. Driven by an effective model for the case of two sets of orthogonal fractures in an isotropic background, we frist express and simplify stiffness parameters in terms of two sets of normal and tangential fracture weaknesses. In the case of a reflection interface separating an isotropic medium and a medium that contains two sets of orthogonal fractures, we present the approximate perturbations in stiffness parameters, which are utilized for the derivation of PP- and PS-wave linearized reflection coefficients. Using the derived PP- and PS-wave reflection coefficients, we establish an inversion approach of joint azimuthal PP- and PS-wave amplitudes variation with incidence angle (AVA) to estimate the normal and tangential fracture weaknesses. In the inversion approach, the least-squares algorithm and Bayesian Markov chain Monte Carlo (MCMC) method are combined, and initial models of fracture weaknesses are built using results of anisotropic AVA gradient. We apply the proposed inversion approach to synthetic seismic data of different signal-to-noise ratios (SNR), and the established inversion approach can provide more accurate normal and tangential fracture weaknesses than the conventional least-squares algorithm even in the case of SNR of 2. Applying the inversion approach to real datasets of PP and PS waves, we obtain reliable results of fracture weaknesses that can match well log curve of velocity and anisotropic AVA gradient, which may provide the possibility to characterize how fractures distribute and to estimate fracture connectivity in hydrocarbon reservoirs.

## INTRODUCTION

Underground fractures usually exist in the form of networks. Estimation of fracture connectivity is an important task in the detection and characterization of fractured reservoirs. In the case of two orthogonal fracture sets in an isotropic background rock, Bakulin et al. (2000b) present how to compute stiffness parameters using two sets of normal and tangential fracture weaknesses ($\delta_{N1}$ and $\delta_{T1}$, and $\delta_{N2}$ and $\delta_{T2}$). Rock physics modeling show that fracture connectivity can reduce seismic wave velocity anisotropy, and in the case of fluid-filled fractures, rock stiffness parameters and anisotropy are complex and frequency dependent (Rubino et al., 2017; Guo et al., 2018). However, the effect of fracture connectivity on seismic wave reflection amplitude variation with offset/incidence angle and azimuth (AVOA/AVAZ) remains unexplored, and how to employ features of AVAZ data to estimate fracture connectivity should also be explored.

[*]School of Ocean and Earth Science, Tongji University, Shanghai, China; and CREWES Project, University of Calgary, Calgary, Alberta, Canada. Email: huaizhen.chen@ucalgary.ca

Currently, analysis and inversion of AVAZ features for estimating underground fractures are implemented under the assumption of horizontal transversly isotropic media (HTI) or tilted transversly isotropic media (TTI), i.e. focusing on the media containing one single set of aligned vertical or subvertical fractures. Rüger (1998) derives a PP-wave linearized reflection coefficient for HTI media, which drives the analysis and inversion of PP-wave AVAZ data for the estimation of fractured areas and fracture-related parameters (e.g. fracture weaknesses, anisotropic parameters). Combining azimuthal AVO and curvature, Hunt et al. (2010) implement quantitative estimate of fracture density based on the near-offset version of Rüger (1998) reflection coefficeint. Downton and Roure (2015) present how to utilize Fourier series of linearized PP-wave reflection coefficient to implement the estimation of fracture symmetry and AVA anisotropic gradient. In a series of papers, Pšenčík and Gajewski (1998), Pšenčík and Vavryčuk (1998) and Vavryčuk and Pšenčík (1998), propose expressions of PP-wave reflection coefficients in terms of weak anisotropy parameters in arbitrary weakly anisotropic media, which may suggest the possibility to calculate reflection coefficients in the case of the rock containing two sets of fractures; however, the complexity of these proposed reflection coefficients limit the application in seismic inversion for estimating fractured reservoirs.

Shear wave splitting exists in fractured media and is utilized to characterize fracture properties (Li and Crampin, 1991; Liu and Martinez, 2014). AVAZ datasets of reflected shear wave has also been employed to implement the inversion for estimating fracture compliances and weaknesses. Again under the assumption of HTI media, Chen et al. (2018) derive a linearized reflection coefficient of PS wave and establish an inversion approach of joint inversion of PP- and PS-wave AVAZ data to estimate fracture weaknesses and compliances. However, in the case of the rock containing two sets of orthogonal fractures, the effect of fracture connectivity on S wave reflection amplitude also remains unexplored. To derive reflection coefficients in anisotropic media, Shaw and Sen (2006) present relationships between PP- and PS-wave reflection coefficients and scattering potentials, which provide the possiblity to derive PS-wave reflection coefficient in the media containing two sets of orthogonal fractures.

Based on the effective model proposed by Bakulin et al. (2000b), we express the simplified stiffness parameters of the medium containing two sets of orthogonal fractures and perturbations in stiffness parameters across a reflection interface. Using the expression of PP-wave given by Pšenčík and Vavryčuk (1998) for arbitrary anisotropic media and the relationship between PS-wave and the scattering potential, we derive linearized PP- and PS-wave reflection coefficients in terms of two sets of normal and tangential fracture weaknesses. Based on the derived reflection coefficients, we present an inversion approach and workflow of joint inversion of PP- and PS-wave AVAZ datasets to estimate two sets of fracture weaknesses, in which we combine the least-squares (LS) inversion algorithm and Bayesian Markov chain Monte Carlo (MCMC) method to obtain acceptable candidates of unknown parameter vector involving fracture weaknesses. We first apply the inversion approach to synthetic data to verify the stability and robustness, and then we employ processed real datasets of PP and PS waves to estimate two sets of fracture weaknesses, which reveals that the proposed inversion approach may generate reliable results of fracture weaknesses that can be used for the characterization of fractured reservoirs and provides the possibility to estimate fracture connectivity.

## THEORY AND METHOD

We focus on the case of fractured rock that is composed of two orthogonal sets of vertical fractures embedded in an isotropic background, as shown in Figure 1.
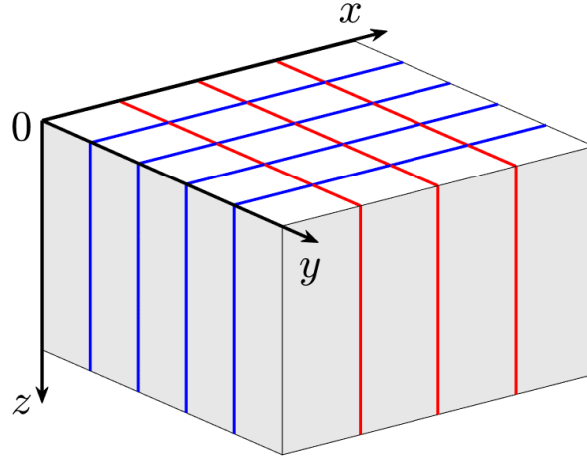


FIG. 1. A model of fractured rock consisting of two orthogonal sets of vertical fractures. Blue lines represent the set of primary fractures, and red lines represent the set of second fractures.

In this section, we explain how to obtain simplified and approximate stiffness matrix of the fractured rock. Using the simplified stiffness matrix we derive P-to-P reflection coefficient as a function of fracture weaknesses. Based on the derived reflection coefficient, we establish an approach and workflow of employing observed seismic data of different azimuthal angles to estimate fracture weaknesses.

### Perturbations in stiffness parameters of rocks with two orthogonal sets of fractures

Under assumptions that fractures are rotationally invariant and the background rock is isotropic, Bakulin et al. (2000b) proposed the effective stiffness matrix $\mathbf{C}$ of the rock with two orthogonal sets of vertical fractures

$$
\mathbf{C} = \begin{bmatrix}
C_{11} & C_{12} & C_{13} & 0 & 0 & 0 \\
C_{12} & C_{22} & C_{23} & 0 & 0 & 0 \\
C_{13} & C_{23} & C_{33} & 0 & 0 & 0 \\
0 & 0 & 0 & C_{44} & 0 & 0 \\
0 & 0 & 0 & 0 & C_{55} & 0 \\
0 & 0 & 0 & 0 & 0 & C_{66}
\end{bmatrix}
$$
$$
= \begin{bmatrix}
\frac{Ml_1m_3}{d} & \frac{\lambda l_1 m_1}{d} & \frac{\lambda l_1 m_2}{d} & 0 & 0 & 0 \\
\frac{\lambda l_1 m_1}{d} & \frac{Ml_3 m_1}{d} & \frac{\lambda l_2 m_1}{d} & 0 & 0 & 0 \\
\frac{\lambda l_1 m_2}{d} & \frac{\lambda l_2 m_1}{d} & \frac{M(l_3 m_3 - l_4)}{d} & 0 & 0 & 0 \\
0 & 0 & 0 & \mu\left(1 - \delta_{T2}\right) & 0 & 0 \\
0 & 0 & 0 & 0 & \mu\left(1 - \delta_{T1}\right) & 0 \\
0 & 0 & 0 & 0 & 0 & \mu\frac{(1-\delta_{T1})(1-\delta_{T2})}{1-\delta_{T1}\delta_{T2}}
\end{bmatrix},
$$

(1)

where $\lambda$ and $\mu$ are Lamé parameters of the isotropic background, $M = \lambda + 2\mu$, and

$$l_1 = 1 - \delta_{N1},$$

$$l_2 = 1 - (1 - 2g)\,\delta_{N1},$$

$$l_3 = 1 - (1 - 2g)^2\,\delta_{N1},$$

$$l_4 = 4\,(1 - 2g)^2\,g^2\delta_{N1}\delta_{N2},$$

$$m_1 = 1 - \delta_{N2},$$

$$m_2 = 1 - (1 - 2g)\,\delta_{N2},$$

$$m_3 = 1 - (1 - 2g)^2\,\delta_{N2},$$

$$d = 1 - (1 - 2g)^2\,\delta_{N1}\delta_{N2}, \tag{2}$$

and where

$$g = \frac{\mu}{M}, \tag{3}$$

and $\delta_{N1}$, $\delta_{N2}$, $\delta_{T1}$ and $\delta_{T2}$ are the normal and tangential fracture weaknesses related to two orthogonal sets of vertical fractures (Bakulin et al., 2000b). Assuming the normal and tangential fracture weaknesses are relatively small (i.e. $0 \leq \delta_{N1}, \delta_{N2}, \delta_{T1}, \delta_{T2} < 1$), we neglect the term proportional to $\delta_{N1}\delta_{N2}$ and $\delta_{T1}\delta_{T2}$; hence, the stiffness parameters are simplified as

$$C_{11} \approx M\left[1 - \delta_{N1} - (1 - 2g)^2\,\delta_{N2}\right],$$

$$C_{12} \approx \lambda\left(1 - \delta_{N1} - \delta_{N2}\right),$$

$$C_{13} \approx \lambda\left[1 - \delta_{N1} - (1 - 2g)\,\delta_{N2}\right],$$

$$C_{22} \approx M\left[1 - (1 - 2g)^2\,\delta_{N1} - \delta_{N2}\right],$$

$$C_{23} \approx \lambda\left[1 - (1 - 2g)\,\delta_{N1} - \delta_{N2}\right],$$

$$C_{33} \approx M\left[1 - (1 - 2g)^2\,\delta_{N1} - (1 - 2g)^2\,\delta_{N2}\right],$$

$$C_{44} = \mu\left(1 - \delta_{T2}\right),$$

$$C_{55} = \mu\left(1 - \delta_{T1}\right),$$

$$C_{66} \approx \mu\left(1 - \delta_{T1} - \delta_{T2}\right). \tag{4}$$

Using the simplified stiffness parameters, we proceed to the derivation of reflection coefficients for an interface that separates an isotropic layer and a fractured layer. We first express perturbations in stiffness parameters across the interface as

$$\Delta C_{11} \approx \Delta M - M\delta_{N1} - M\left(1 - 2g\right)^2\,\delta_{N2},$$

$$\Delta C_{12} \approx \Delta\lambda - \lambda\delta_{N1} - \lambda\delta_{N2},$$

$$\Delta C_{13} \approx \Delta\lambda - \lambda\delta_{N1} - \lambda\left(1 - 2g\right)\delta_{N2},$$

$$\Delta C_{22} \approx \Delta M - M\left(1 - 2g\right)^2\delta_{N1} - M\delta_{N2},$$

$$\Delta C_{23} \approx \Delta\lambda - \lambda\left(1 - 2g\right)\delta_{N1} - \lambda\delta_{N2},$$

$$\Delta C_{33} \approx \Delta M - M\left(1 - 2g\right)^2\delta_{N1} - M\left(1 - 2g\right)^2\delta_{N2},$$

$$\Delta C_{44} = \Delta\mu - \mu\delta_{T2},$$

$$\Delta C_{55} = \Delta\mu - \mu\delta_{T1},$$

$$\Delta C_{66} \approx \Delta\mu - \mu\delta_{T1} - \mu\delta_{T2}, \tag{5}$$

where $\Delta M$ and $\Delta\mu$ are changes in P- and S-wave moduli across the interface, and we stress that in the perturbations we neglect the term that is proportional to $\Delta M\delta_{N1}$, $\Delta M\delta_{N2}$, $\Delta\lambda\delta_{N1}$, $\Delta\lambda\delta_{N2}$, $\Delta\mu\delta_{T1}$ and $\Delta\mu\delta_{T2}$ again under the assumptions that changes in both elastic parameters ($M$, $\mu$, and $\lambda$) across the interface and two sets of fracture weaknesses are small.

## Parameterization of P-to-P and P-to-S reflection coefficients

Following Pšenčík and Gajewski (1998), Pšenčík and Vavryčuk (1998) and Vavryčuk and Pšenčík (1998), we first use the expressed perturbations in stiffness parameters to derive the P-to-P reflection coefficient $R_{\mathrm{PP}}(\theta, \phi)$ as the sum of isotropic part $R_{\mathrm{PP}}^{\mathrm{iso}}(\theta)$ related to background rock elastic parameters and anisotropic part $R_{\mathrm{PP}}^{\mathrm{ani}}(\theta, \phi)$ related to two sets of fracture weaknesses (Appendix A)

$$R_{\mathrm{PP}}\left(\theta, \phi\right) = R_{\mathrm{PP}}^{\mathrm{iso}}\left(\theta\right) + R_{\mathrm{PP}}^{\mathrm{ani}}\left(\theta, \phi\right), \tag{6}$$

where

$$R_{\mathrm{PP}}^{\mathrm{iso}}\left(\theta\right) = a_{\rho}\left(\theta\right)\frac{\Delta\rho}{\rho} + a_{M}\left(\theta\right)\frac{\Delta M}{M} + a_{\mu}\left(\theta\right)\frac{\Delta\mu}{\mu},$$

$$\begin{aligned} R_{\mathrm{PP}}^{\mathrm{ani}}\left(\theta, \phi\right) = & a_{N1}\left(\theta, \phi\right)\delta_{N1} + a_{N2}\left(\theta, \phi\right)\delta_{N2} \\ & + a_{T1}\left(\theta, \phi\right)\delta_{T1} + a_{T2}\left(\theta, \phi\right)\delta_{T2}, \end{aligned} \tag{7}$$

in which $\rho$ is density, $\Delta\rho$ is the perturbation in density across the reflection interface, and

$$a_{\rho}\left(\theta\right) = \frac{1}{4}\frac{\cos 2\theta}{\cos^2\theta},$$

$$a_{M}\left(\theta\right) = \frac{1}{4}\sec^2\theta,$$

$$a_{\mu}\left(\theta\right) = -2g\sin^2\theta,$$

$$\begin{aligned} a_{N1}\left(\theta, \phi\right) = & -\frac{1}{4}\left[\left(1 - 2g\right)\cos\theta + \cos^2\phi\sin\theta\tan\theta\right]^2 \\ & -\frac{\left(1 - 2g\right)}{2}\left[\begin{array}{l}\sec^2\theta - \frac{1}{2}\sin^2\phi\tan^2\theta \\ -g\left(2 + \sin^2\phi\tan^2\theta\right)\end{array}\right]\sin^2\theta\sin^2\phi, \end{aligned}$$

$$a_{N2}(\theta, \phi) = -\frac{1}{4}\left[(1-2g)\cos\theta + \sin^2\phi\sin\theta\tan\theta\right]^2$$

$$-\frac{(1-2g)}{2}\left[\begin{array}{c}\sec^2\theta - \frac{1}{2}\cos^2\phi\tan^2\theta\\ -g\left(2 + \cos^2\phi\tan^2\theta\right)\end{array}\right]\sin^2\theta\cos^2\phi,$$

$$a_{T1}(\theta, \phi) = g\cos^2\phi\sin^2\theta\left(1 - \sin^2\phi\tan^2\theta\right),$$

$$a_{T2}(\theta, \phi) = g\sin^2\phi\sin^2\theta\left(1 - \cos^2\phi\tan^2\theta\right), \tag{8}$$

where $\theta$ is the incidence angle of P-wave, and $\phi$ is the azimuth, which is equal to zero in the $(x, z)$ plane.

Following Shaw and Sen (2006) and Chen et al. (2018), we next utilize the perturbations in stiffness parameters again to derive the reflection coefficient of P-to-S wave using the scattering potential $\mathcal{S}_{\mathrm{PS}}$. The P-to-S reflection coefficient is given by

$$R_{\mathrm{PS}} = \frac{\sin\theta}{2\rho\cos\psi\sin(\theta+\psi)}\mathcal{S}_{\mathrm{PS}}, \tag{9}$$

where $\psi$ is the angle of reflected S-wave, and $\mathcal{S}_{\mathrm{PS}}$ is expressed as

$$\mathcal{S}_{\mathrm{PS}} = \Delta\rho\cos2\theta + \sum_{i=1,j=1}^{i=6,j=6}\Delta C_{ij}\eta_{ij}, \tag{10}$$

where $\Delta C_{ij}$ represents the perturbation is stiffness parameter, and $\eta_{ij}$ is related to reflected P- and S-wave angle and azimuthal angle (Appendix A).

Combining equations 9 and 10, we derive the P-to-S reflection coefficient as

$$R_{\mathrm{PS}}(\theta, \phi) = R_{\mathrm{PS}}^{\mathrm{iso}}(\theta) + R_{\mathrm{PS}}^{\mathrm{ani}}(\theta, \phi) \tag{11}$$

where

$$R_{\mathrm{PS}}^{\mathrm{iso}}(\theta) = b_\mu(\theta)\frac{\Delta\mu}{\mu} + b_\rho(\theta)\frac{\Delta\rho}{\rho}$$

$$R_{\mathrm{PS}}^{\mathrm{ani}}(\theta, \phi) = b_{N1}(\theta, \phi)\delta_{N1} + b_{N2}(\theta, \phi)\delta_{N2}$$
$$+ b_{T1}(\theta, \phi)\delta_{T1} + b_{T2}(\theta, \phi)\delta_{T2}, \tag{12}$$

and where

$$b_\mu(\theta) = \sqrt{g}\frac{\sin\theta\left(\sin2\psi + \sin2\theta\cos2\psi\right)}{2\cos\psi\sin(\theta+\psi)},$$

$$b_\rho(\theta) = \frac{\sin\theta\cos2\theta}{2\cos\psi\sin(\theta+\psi)},$$

$$b_{N1}(\theta, \phi) = \frac{1}{\sqrt{g}}\frac{\sin\theta\sin\psi\cos^2\phi}{\sin(\theta+\psi)}\left[\sin^2\theta\cos^2\phi\left(1-2g^2\right) - g\left(1-2g\right)\right],$$

$$b_{N2}(\theta, \phi) = -\sqrt{g}\frac{\sin\theta\sin\psi\sin^2\phi}{\sin(\theta+\psi)}\left[2g\sin^2\theta\sin^2\phi + (1-2g)\right],$$

$$b_{T1}(\theta, \phi) = \sqrt{g}\frac{\sin\theta\cos^2\phi}{2\cos\psi\sin(\theta+\psi)}\left(\sin 2\theta\cos 2\psi - 2\sin^2\theta\sin 2\psi\sin^2\phi\right),$$

$$b_{T2}(\theta, \phi) = \sqrt{g}\frac{\sin\theta\sin^2\phi}{2\cos\psi\sin(\theta+\psi)}\left(\sin 2\theta\cos 2\psi - 2\sin^2\theta\sin 2\psi\cos^2\phi\right). \qquad (13)$$

Based on the Snell's law, the relationship between angles of incident P-wave and reflected S-wave ($\theta$ and $\psi$) is given by

$$\frac{\sin\theta}{\alpha} = \frac{\sin\psi}{\beta}. \qquad (14)$$

**Inversion of differences in azimuthal amplitudes for fracture weaknesses**

Following Bakulin et al. (2000a), we express the normal and tangential fracture weaknesses for fluid saturated fractures under the assumption that there are no interaction between two sets of fractures, which indicates that we may utilize fracture density values $e_1$ and $e_2$ to compute the corresponding normal and tangential fracture weaknesses

$$\delta_{N1} = \frac{4e_1}{3g(1-g)\left[1+\frac{1}{\pi g(1-g)}\frac{K_f}{\mu\chi_1}\right]},$$

$$\delta_{T1} = \frac{16e_1}{3(3-2g)},$$

$$\delta_{N2} = \frac{4e_2}{3g(1-g)\left[1+\frac{1}{\pi g(1-g)}\frac{K_f}{\mu\chi_2}\right]},$$

$$\delta_{T2} = \frac{16e_2}{3(3-2g)}, \qquad (15)$$

where $\chi_1$ and $\chi_2$ are aspect ratios of two sets of fractures. We emphasize that we assume the fluid is evenly filled in two sets of fractures. Given different values of fracture density, we plot how the normal fracture weakness $\delta_N$ varies with fracture aspect ratio $\alpha$ for the case of gas-bearing fractures in Figure 2. We observe that given a certain fracture density and water saturation for gas-bearing fractures, the normal fracture weakness is approximately constant in the case of fracture aspect ratio being in $0.001 - 0.01$, which means the effect of fracture aspect ratio on $\delta_N$ can be neglected and $\delta_N$ changes significantly with fracture density $e$. Hence, we may rewrite two sets of fracture weaknesses as

$$\delta_{N1} = \gamma\delta_{N2},$$

$$\delta_{T1} = \gamma\delta_{T2}, \qquad (16)$$

where $\gamma = \frac{e_1}{e_2}$ is fracture density ratio, which may be obtained using well logging and core data.

Based on the derived linearized reflection coefficients of PP and PS waves, we next present how to employ PP- and PS-wave amplitude variations with incidence and azimuthal
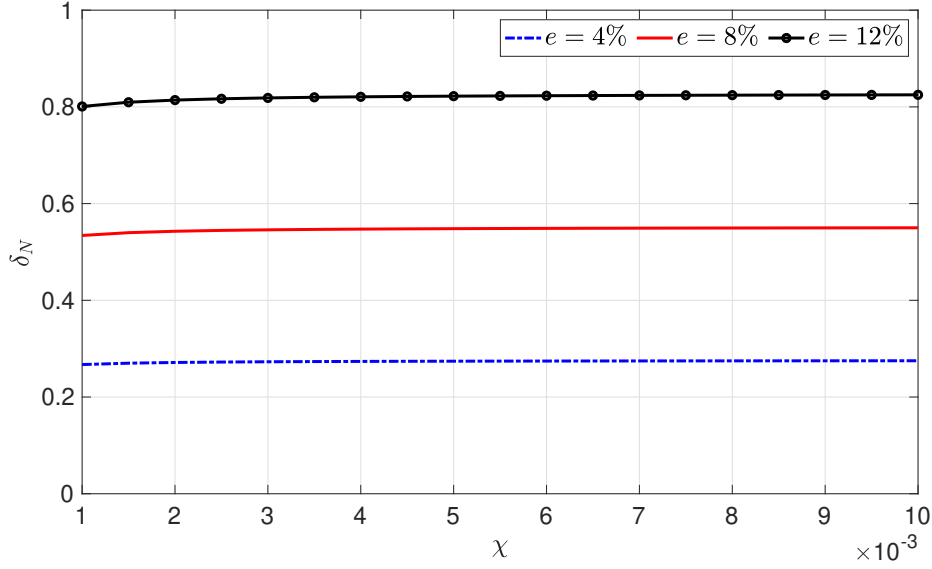
FIG. 2. Variations of normal fracture weakness with aspect ratio in the case of different values of fracture density (water saturation $S_{\mathrm{w}} = 50\%$).

angles (AVAZ) to estimate fracture weaknesses. In the case that we have pre-stacked PP- and PS-wave seismic datasets of two azimuthal angles $\phi_1$ and $\phi_k$, differences in reflection coefficients of two azimuthal angles for PP and PS waves are respectively expressed as

$$\Delta R_{\mathrm{PP}}\left(\theta, \phi_1, \phi_k\right) = \mathcal{P}_N\left(\theta, \phi_1, \phi_k\right)\delta_{N2} + \mathcal{P}_T\left(\theta, \phi_1, \phi_k\right)\delta_{T2},$$

$$\Delta R_{\mathrm{PS}}\left(\theta, \phi_1, \phi_k\right) = \mathcal{Q}_N\left(\theta, \phi_1, \phi_k\right)\delta_{N2} + \mathcal{Q}_T\left(\theta, \phi_1, \phi_k\right)\delta_{T2}, \quad (17)$$

where

$$\mathcal{P}_N\left(\theta, \phi_1, \phi_k\right) = \gamma A_{N1}\left(\theta, \phi_1, \phi_k\right) + A_{N2}\left(\theta, \phi_1, \phi_k\right),$$

$$\mathcal{P}_T\left(\theta, \phi_1, \phi_k\right) = \gamma A_{T1}\left(\theta, \phi_1, \phi_k\right) + A_{T2}\left(\theta, \phi_1, \phi_k\right),$$

$$\mathcal{Q}_N\left(\theta, \phi_1, \phi_k\right) = \gamma B_{N1}\left(\theta, \phi_1, \phi_k\right) + B_{N2}\left(\theta, \phi_1, \phi_k\right),$$

$$\mathcal{Q}_T\left(\theta, \phi_1, \phi_k\right) = \gamma B_{T1}\left(\theta, \phi_1, \phi_k\right) + B_{T2}\left(\theta, \phi_1, \phi_k\right), \quad (18)$$

and where

$$A_{N1}\left(\theta, \phi_1, \phi_k\right) = a_{N1}\left(\theta, \phi_k\right) - a_{N1}\left(\theta, \phi_1\right),$$

$$A_{N2}\left(\theta, \phi_1, \phi_k\right) = a_{N2}\left(\theta, \phi_k\right) - a_{N2}\left(\theta, \phi_1\right),$$

$$A_{T1}\left(\theta, \phi_1, \phi_k\right) = a_{T1}\left(\theta, \phi_k\right) - a_{T1}\left(\theta, \phi_1\right),$$

$$A_{T2}\left(\theta, \phi_1, \phi_k\right) = a_{T2}\left(\theta, \phi_k\right) - a_{T2}\left(\theta, \phi_1\right),$$

$$B_{N1}\left(\theta, \phi_1, \phi_k\right) = b_{N1}\left(\theta, \phi_k\right) - b_{N1}\left(\theta, \phi_1\right),$$

$$B_{N2}\left(\theta, \phi_1, \phi_k\right) = b_{N2}\left(\theta, \phi_k\right) - b_{N2}\left(\theta, \phi_1\right),$$

$$B_{T1}\left(\theta, \phi_1, \phi_k\right) = b_{T1}\left(\theta, \phi_k\right) - b_{T1}\left(\theta, \phi_1\right),$$

$$B_{T2}\left(\theta, \phi_1, \phi_k\right) = b_{T2}\left(\theta, \phi_k\right) - b_{T2}\left(\theta, \phi_1\right). \tag{19}$$

Using the corresponding wavelets $W_{\text{PP}}$ and $W_{\text{PS}}$, we express difference in azimuthal seismic amplitudes as

$$\begin{bmatrix} \Delta S_{\text{PP}}\left(\theta, \phi_1, \phi_k\right) \\ \Delta S_{\text{PS}}\left(\theta, \phi_1, \phi_k\right) \end{bmatrix} = \begin{bmatrix} W_{\text{PP}}\,\mathcal{P}_N\left(\theta, \phi_1, \phi_k\right) & W_{\text{PP}}\,\mathcal{P}_T\left(\theta, \phi_1, \phi_k\right) \\ W_{\text{PS}}\,\mathcal{Q}_N\left(\theta, \phi_1, \phi_k\right) & W_{\text{PS}}\,\mathcal{Q}_T\left(\theta, \phi_1, \phi_k\right) \end{bmatrix} \begin{bmatrix} \delta_{N2} \\ \delta_{T2} \end{bmatrix}, \tag{20}$$

which is written succinctly as

$$\mathbf{d} = \mathbf{Gm}. \tag{21}$$

To solve the inversion problem, we establish a Bayesian Markov chain Monte Carlo (MCMC) approach to obtain the acceptable results of the unknown parameter vector $\mathbf{m}$. In the Bayes' theorem, the posterior probability distribution function (PDF), $P\left(\mathbf{m}|\mathbf{d}\right)$, is proportional to the likelihood function $P\left(\mathbf{d}|\mathbf{m}\right)$ and the prior PDF $P\left(\mathbf{m}\right)$

$$P\left(\mathbf{m}|\mathbf{d}\right) \propto P\left(\mathbf{d}|\mathbf{m}\right) P\left(\mathbf{m}\right), \tag{22}$$

where the likelihood function is expressed as

$$P\left(\mathbf{d}|\mathbf{m}\right) \propto \exp\left(-\frac{\left(\mathbf{d} - \mathbf{Gm}\right)^T\left(\mathbf{d} - \mathbf{Gm}\right)}{2\sigma_{\text{noise}}^2}\right), \tag{23}$$

and the prior PDF is given by

$$P\left(\mathbf{m}\right) \propto \exp\left(-\frac{\left(\mathbf{m} - m_{\text{a}}\right)^T\left(\mathbf{m} - m_{\text{a}}\right)}{2\sigma_{\mathbf{m}}^2}\right), \tag{24}$$

under assumptions that both the noise and the priori are Gaussian, $\sigma_{\text{noise}}^2$ and $\sigma_{\mathbf{m}}^2$ represent the variances of noise and model parameter vector, and $m_{\text{a}}$ represents the average value of $\mathbf{m}$. The Metropolis-Hasting algorithm is employed to implement the Bayesian MCMC inversion for estimating the unknown parameter vector, which involves two steps:

1) Generate a candidate vector $\mathbf{m}^*$ by perturbating the current model vector $\mathbf{m}$;

2) Determine if the obtained candidate vector can be accepted by comparing a probability computed by

$$\xi = \min\left[1, \frac{P\left(\mathbf{m}^*|\mathbf{d}\right)}{P\left(\mathbf{m}|\mathbf{d}\right)}\right], \tag{25}$$

with a random number $\Gamma \in [0, 1]$. We accept the candidate in the case of $\xi > \Gamma$; otherwise, we reject the candidate and generate a new candidate again perturbating the model vector $\mathbf{m}$.

We employ the Newton algorithm to generate the candidate vector

$$\mathbf{m}_{i+1} = \mathbf{m}_i + \nu \Delta \mathbf{m}, \tag{26}$$

where $\nu \in [0, 1]$ is a random number, and $\Delta \mathbf{m}$ is the perturbation in unknown parameter vector, which is computed using the least-squares (LS) method

$$\Delta \mathbf{m} = \left(\mathbf{G}^T \mathbf{G}\right)^{-1} \mathbf{G}^T \left(\mathbf{d} - \mathbf{G}\, \mathbf{m}_i\right). \tag{27}$$

We emphasize that we combine the least-squares method and Bayesian MCMC algorithm to generate a few of acceptable candidates for estimate the unknown parameter vector $\mathbf{m}$, and the average value of all the acceptable candidates is preserved as the final inversion result.

## NUMERICAL EXAMPLES

In this section, we first analyze AVAZ features of PP- and PS-wave reflection coefficients for the case of the rock containing one or two sets of fractures respectively, and then we employ synthetic seismic data of different signal-to-noise ratios (SNR) and real data sets to test the stability and reliability of the proposed inversion approach.

### Analysis of PP- and PS-wave reflection coefficient AVAZ features

In the case of an reflection interface separating an isotropic sand layer and a fractured shale layer, we compute PP- and PS-wave reflection coefficients using the derived equations 6 and 11). Assuming the shale layer contains one and two sets of factures respectively, we compute PP- and PS-wave reflection coefficients for the reflection interface. For the gas-saturated fractures (i.e. Let $K_f = 0.02$ GPa), we compute the frature weaknesses using equation 15. Elastic parameters (P- and S-wave moduli), density and fracture weaknesses are shown in Table 2, in which we use $e_1 = 0$ and $e_2 = 0.15$ for the case of shale containing one set of fractures, and use $e_1 = 0.02$ and $e_2 = 0.15$ for that of shale containing two sets of fracture weaknsses. We assume the same aspect ratio for fractures, i.e. $\chi_1 = \chi_2 = 0.01$. In Figure 3, we focus on how anisotropic parts of PP- and PS-wave reflection coefficients vary with incidence and azimuthal angles since the isotropic parts have no change for two cases of fractured shale layer.

Table 1. Parameters of sand-shale model

| | $M$ (GPa) | $\mu$ (GPa) | $\rho$ (g/cm$^3$) | $\delta_{N1}$ | $\delta_{T1}$ | $\delta_{N2}$ | $\delta_{T2}$ |
|---|---|---|---|---|---|---|---|
| Sand | 83 | 33 | 2.65 | 0 | 0 | 0 | 0 |
| Shale (one set) | 37 | 9 | 2.55 | 0 | 0 | 0.7849 | 0.3183 |
| Shale (two sets) | 37 | 9 | 2.55 | 0.1047 | 0.0424 | 0.7849 | 0.3183 |

Table 2. Parameters of sand-shale model

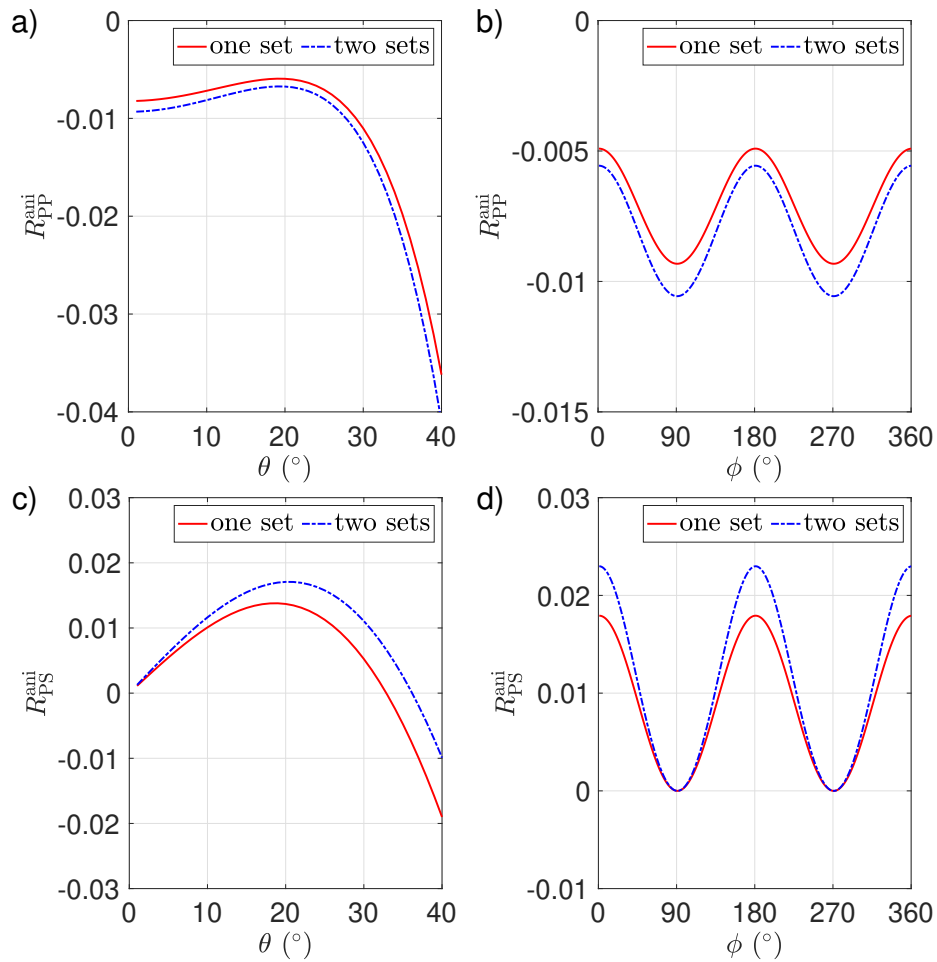|  | $\delta_{N1}$ | $\delta_{T1}$ | $\delta_{N2}$ | $\delta_{T2}$ |
|---|---|---|---|---|
| Sand | 0 | 0 | 0 | 0 |
| Shale (one set) | 0 | 0 | 0.7849 | 0.3183 |
| Shale (two sets) | 0.1047 | 0.0424 | 0.7849 | 0.3183 |



FIG. 3. Variations of PP- and PS-wave reflection coefficients with incidence and azimuthal angles. a) $R_{PP}(\theta, \phi = 30°)$, b) $R_{PP}(\theta = 20°, \phi)$, c) $R_{PS}(\theta, \phi = 30°)$, d) $R_{PS}(\theta = 20°, \phi)$

We observe that the additional set of fractures only changes the value of PP- and PS-wave reflection coefficients; however, it has no effect on the AVAZ features of PP- and PS-wave reflection coefficients.

## Verification of robustness and stability of the inversion approach

In Figure 4a, we show curves of different values of fracture densities $e_1$ and $e_2$, and under the assumption of gas-bearing fractures (i.e. the fluid in fractures is a mixture of water and gas), we use a given curve of water saturation $S_W$ to compute fluid bulk modulus $K_f$. Using equation 15, we calculate two sets of fracture weaknesses ($\delta_{N1}$, $\delta_{T1}$, and $\delta_{N2}$, $\delta_{T2}$), as shown in Figure 4b.
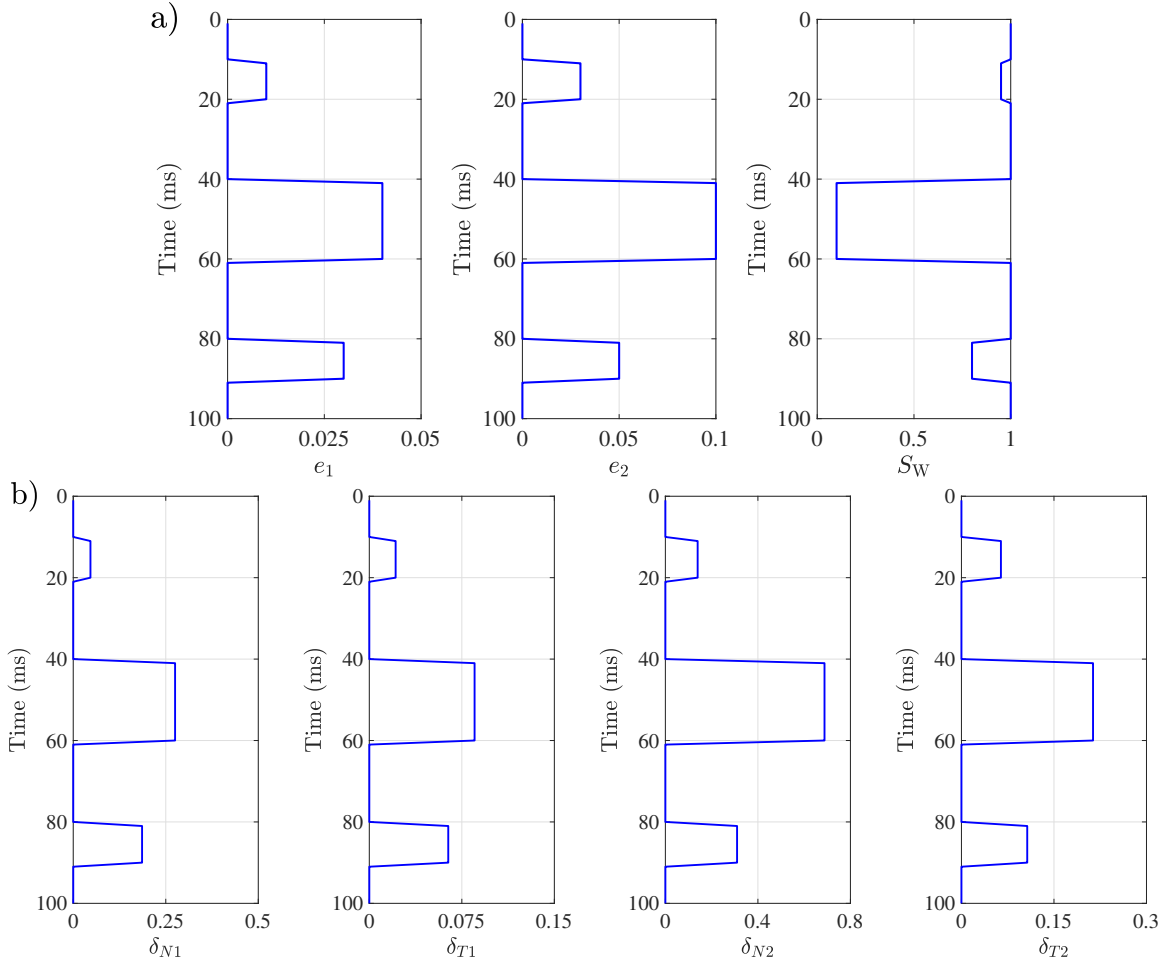


FIG. 4. a) Curves of fracture densities $e_1$ and $e_2$ and water saturation $S_W$, and b) Curves of two sets of calculated fracture weaknesses.

We next use a Ricker wavelet of dominant frequency 25Hz to directly generate differences in azimuthal seismic datasets based on the derived PP- and PS-wave reflection coefficients. Given azimuthal angles of $\phi_1 = 0°$, $\phi_2 = 45°$ and $\phi_3 = 90°$ and incidence angle range of $25° \leq \theta \leq 35°$, we plot differences in azimuthal PP- and PS-wave seismic amplitudes in Figure 5. To testify the robustness of the proposed inversion approach, we add random noise that is assumed to be Gaussian into the synthetic data to produce noisy seismic data of signal-to-noise ratio (SNR) of 5 and 2, respectively. We emphasize that we use the same wavelet for generating PP- and PS-wave amplitudes.

Inputing the generated PP- and PS-wave azimuthal amplitude difference datasets, we

implement the estimation of unknown parameter vector $\mathbf{m}$ using the established inversion approach. In Figure 6a and b), we plot comparisons between all the acceptable inversion results generated using Bayesian MCMC method, initial values, true values, results obtained using the LS algorithm, and the final inversion results computed using all the acceptable inversion results of fracture weaknesses $\delta_{N2}$ and $\delta_{T2}$ in the case of SNR of 5 and 2, respectively. We observe that the final inverted results of fracture weaknesses $\delta_{N2}$ and $\delta_{T2}$
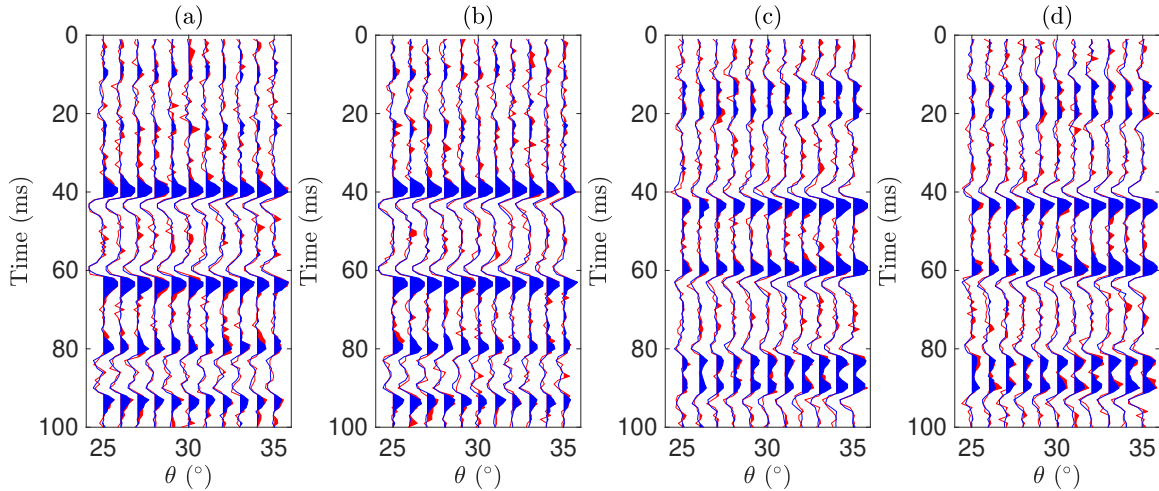


FIG. 5. a) Difference between PP-wave amplitudes of $\phi_1 = 0°$ and $\phi_2 = 45°$; b) Difference between PP-wave amplitudes of $\phi_1 = 0°$ and $\phi_3 = 90°$; c) Difference between PS-wave amplitudes of $\phi_1 = 0°$ and $\phi_2 = 45°$; b) Difference between PS-wave amplitudes of $\phi_1 = 0°$ and $\phi_3 = 90°$. The azimuthal seismic amplitude difference of SNR of 5 is shown in blue, and the azimuthal seismic amplitude difference of SNR of 2 is shown in red.

calculated using all the acceptable results generated using the proposed Bayesian MCMC inversion method can match the true values in the case of SNR of 2, and the proposed inversion approach can produce more reliable results of fracture weaknesses than the LS inversion. Using the inversion results of $\delta_{N2}$ and $\delta_{T2}$, we may compute the values of fracture weaknesses $\delta_{N1}$ and $\delta_{T1}$. We compute the fracture weaknesses $\delta_{N1}$ and $\delta_{T1}$ using the inverted fracture weaknesses $\delta_{N2}$ and $\delta_{T2}$ and the value of $\gamma$ computed using fracture densities $e_1$ and $e_2$ shown in Figure 4a, and we compare the computed results and true values of $\delta_{N1}$ and $\delta_{T1}$, as shown in Figure 7. It reveals that the proposed inversion approach is robust and can be used for estimating reliable fracture weaknesses.

## Real data example

Real datasets of azimuthal PP and PS waves are utilized for the further verification of the stability and reliability of the proposed inversion approach. We first plot in-line and cross-line PP-wave angle gathers of azimuthal angles $\theta_1 = 8°$, $\theta_2 = 17°$ and $\theta_3 = 26°$ extracted at the location of well log in Figure 8. We observe around the location of reservoir (around time 1980 ms), seismic reflection amplitude variation with incidence and azimuthal angles (AVAZ) appears, which can be used as the input data for the prediction of two sets of fracture weaknesses.

Following Chen et al. (2017), we first extract PP-wave AVO intercept and gradient using the angle gathers of different azimuths, and then we compute the curve of AVO anisotropic
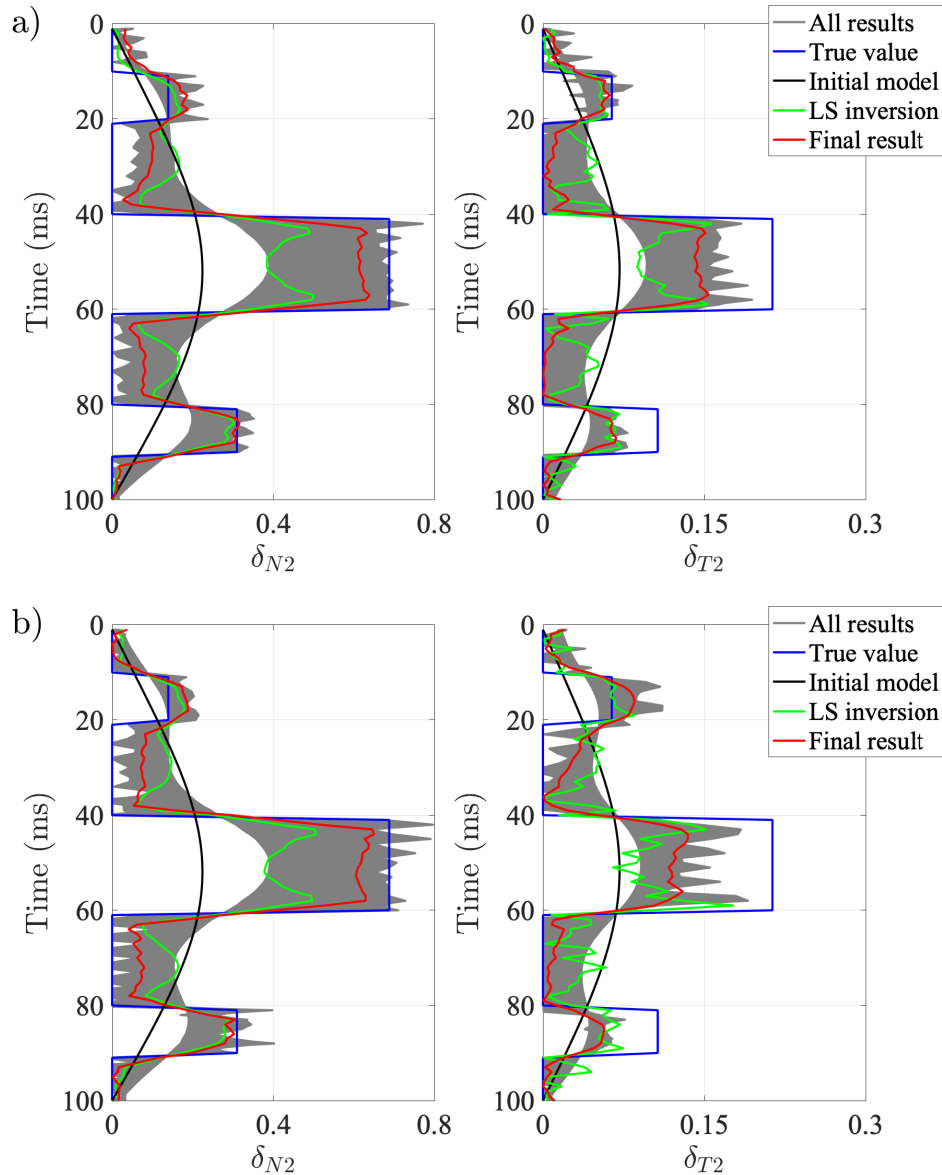
FIG. 6. Comparisons between all the acceptable inversion results generated using Bayesian MCMC method (grey), initial values (black), inversion results estimated using the LS algorithm (green), the final inversion results computed using all the acceptable inversion results (red) of fracture weaknesses $\delta_{N2}$ and $\delta_{T2}$. a) SNR of 5; b) SNR of 2.
r

gradient $B_{\mathrm{ani}}$ at the location of well log. Using the relationship between the normal and tangential fracture weaknesses, we convert the result of $B_{\mathrm{ani}}$ to the tangential fracture weakness $\delta_T$ and compute the fracture density ratio $\gamma$, as shown in Figure 9. We observe there are differences between $B_{\mathrm{ani}}$ results computed using the inline and crossline PP-wave angle gathers at the location of well log, which indicates different sets of fractures may exist at the location where the hydrocarbon reservoir is explored. We also see that at the location of hydrocarbon reservoir, two tangential fracture weaknesses computed using inline and crossline anisotropic gradients shows relatively high values. The calculated fracture density ratio $\gamma$ will be used in the inversion approach to replace the fracture weaknesses $\delta_{N1}$
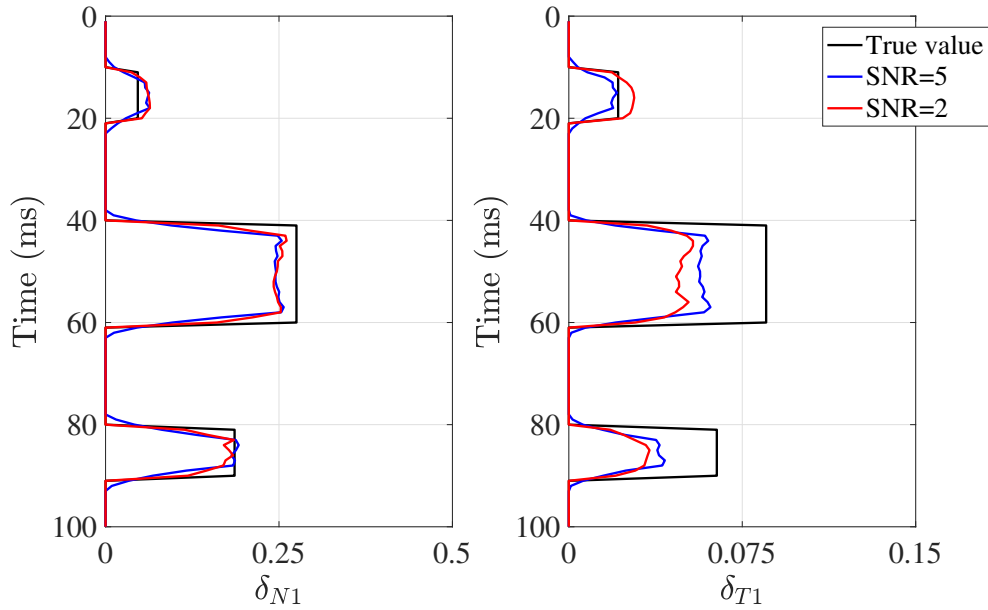
FIG. 7. Compasions true values and inversion results of fracture weaknesses $\delta_{N1}$ and $\delta_{T1}$ for the case of SNR of 5 and 2.
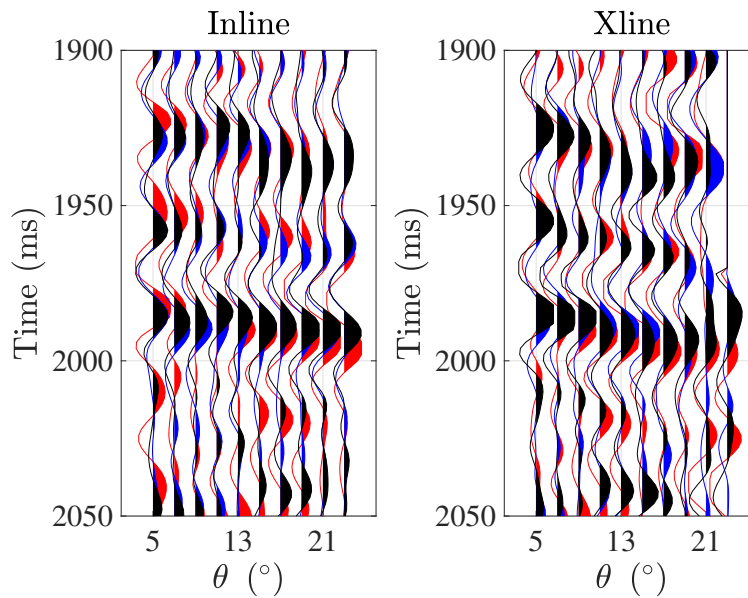


FIG. 8. Inline and crossline PP-wave angle gathers extracted at the location of well log. Seismic profiles plotted in red, blue and black represent angle gathers of azimuths $\phi_1 = 170°$, $\phi_2 = 25°$ and $\phi_3 = 50°$, respectively.

and $\delta_{T1}$ with fracture weaknesses $\delta_{N2}$ and $\delta_{T2}$.

Using the proposed inversion approach, we next estimate the normal and tangential fracture weaknesses $\delta_{N2}$ and $\delta_{T2}$ utilizing PP- and PS-wave AVAZ datasets. We emphasize the input data are differences in azimuthal PP- and PS-wave seismic amplitudes, and instead of using the data of all incidence angles, we employ the partially incidence-angle-stacked seismic amplitudes of the dominant incidence angles $\theta_1 = 8°$, $\theta_2 = 17°$ and $\theta_3 = 26°$ to implement the inversion. In Figure 10, we show the partially incidence-angle-stacked PP-
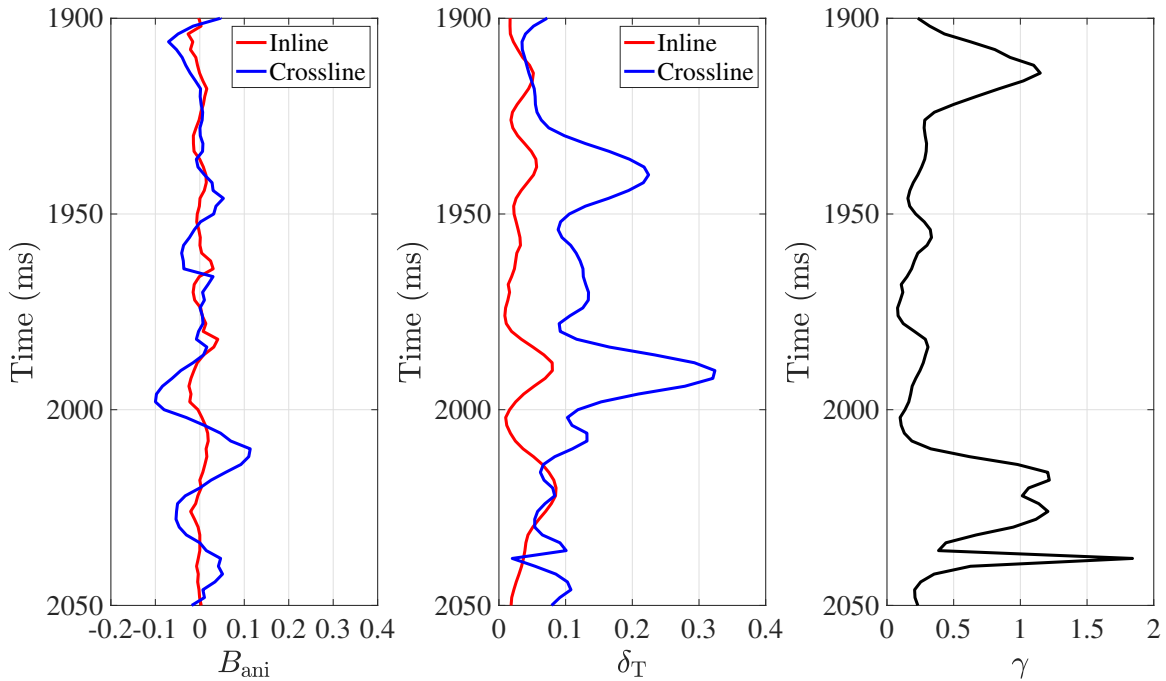
FIG. 9. Anisotropic AVO gradient $B_{\mathrm{ani}}$, tangential fracture weakness $\delta_T$ and fracture density ratio $\gamma$ computed at the location of well log.

and PS-wave seismic data of three incidence angles $\theta_1 = 8°$, $\theta_2 = 17°$ and $\theta_3 = 26°$ and three azimuthal angles $\phi_1 = 170°$, $\phi_2 = 25°$ and $\phi_3 = 50°$.

Initial models of normal and tangential fracture weaknesses $\delta_{N2}$ and $\delta_{T2}$ are built using the computed results of AVO anisotropic gradient $B_{\mathrm{ani}}$, as plotted in Figure 11. Following the proposed inversion approach, we implement the inversion of differences in azimuthal amplitudes of three incidence angles for the normal and tangential fracture weaknesses. Inversion results of the inverted fracture weaknesses are shown in Figure 12. With the inverted fracture weaknesses $\delta_{N2}$ and $\delta_{T2}$ in hand, we next compute the results of $\delta_{N1}$ and $\delta_{T1}$ using the fracture density ratio $\gamma$, as plotted in Figure 13.

We see that at the location of hydrocarbon reservoir, the inverted fracture weaknesses show relatively high values, and the reservior is more distinctly be observed in the inverted results of tangential fracture weaknesses $\delta_{T1}$ and $\delta_{T2}$. Combining two sets of normal and fracture weaknesses provides the possiblity to characterize how fractures distribute and where fractures are connected in the reservoir.

## CONCLUSIONS

Driven by an effective model for rocks containing two sets of orthogonal fractures, we present simplified stiffness parameters in terms of fracture weaknesses and the corresponding perturbations in stiffness parameters across the reflection interface, and then we derive linearized PP- and PS-wave reflection coefficients in terms of two sets of fracture weaknesses. Based on the reflection coefficients, we propose an inversion approach combining the least-squares inversion algorithm and Bayesian Markov chain Monte Carlo (MCMC) method to employ differences in PP- and PS-wave azimuthal amplitudes variation with in-
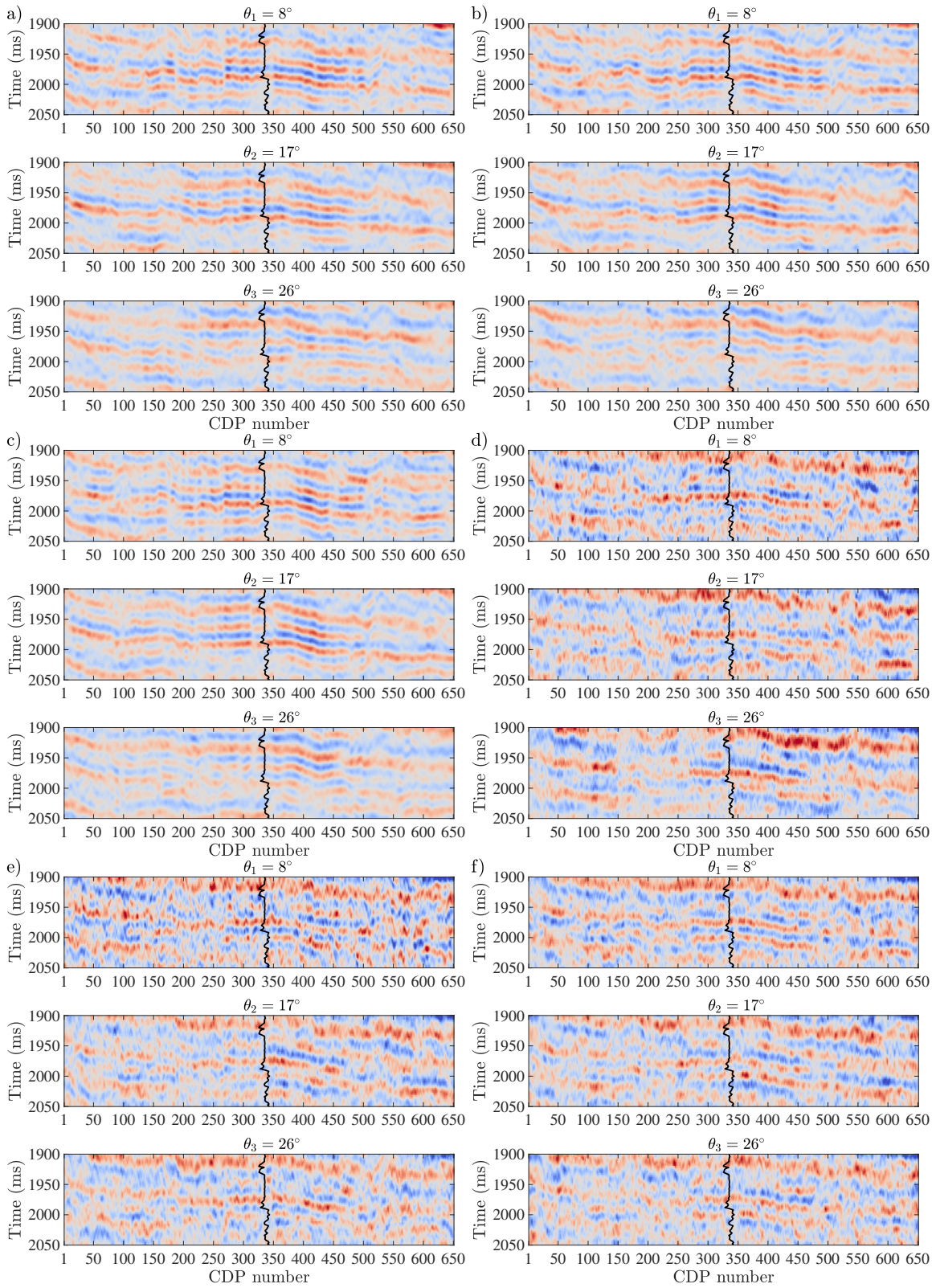
FIG. 10. PP- and PS-wave seismic data of incidence angles $\theta_1 = 8°$, $\theta_2 = 17°$ and $\theta_3 = 26°$. a)-c) PP-wave data of azimuthal angles $\phi_1 = 170°$, $\phi_2 = 25°$ and $\phi_3 = 50°$; and e)-f) PS-wave data of azimuthal angles $\phi_1 = 170°$, $\phi_2 = 25°$ and $\phi_3 = 50°$. The curve is P-wave velocity.
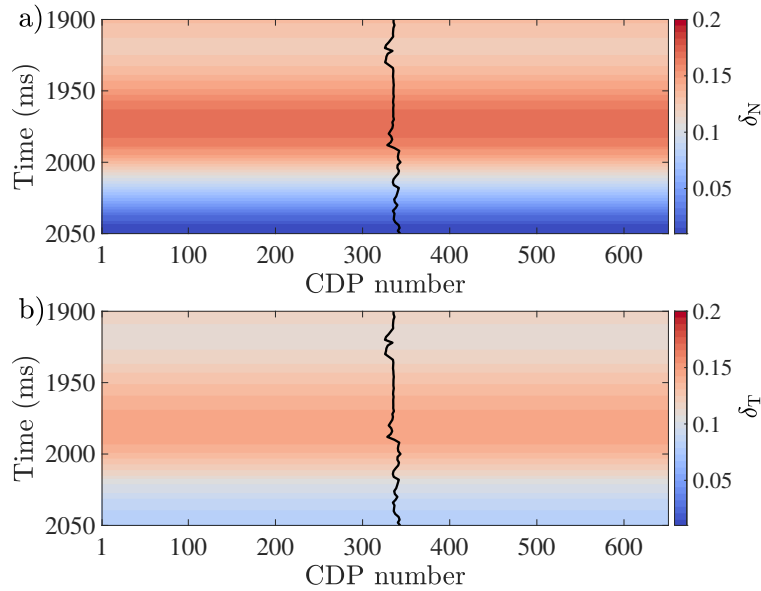
FIG. 11. a) Initial models of the normal fracture weakness $\delta_{N2}$, and b) Initial models of the tangential fracture weakness $\delta_{T2}$. The curve is P-wave velocity.
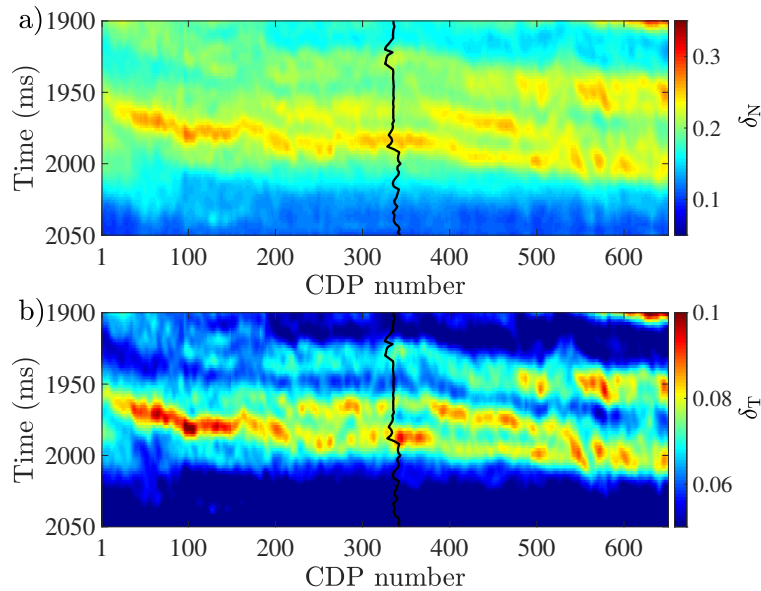


FIG. 12. a) Inversion results of the normal fracture weakness $\delta_{N2}$, and b) Inversion results of the tangential fracture weakness $\delta_{T2}$. The curve is P-wave velocity.

cidence (AVA) to estimate two sets of fracture weaknesses. In the inversion, anisotropic AVA gradients computed using pre-stack seismic data along two different directions is utilized to bulid initial models of two sets of fracture weaknesses and to calculate fracture density ratio.

Applying the proposed inversion and workflow to synthetic seismic datasets of different signal-to-noise ratios (SNR) implies that the normal and tangential fracture weaknesses can be estimated stably in the case of SNR being larger than 2, and the proposed inversion approach can provide more accurate results of fracture weaknesses than the least-squares inverison alogrithm. We finally utilize PP- and PS-wave amplitude datasets of different
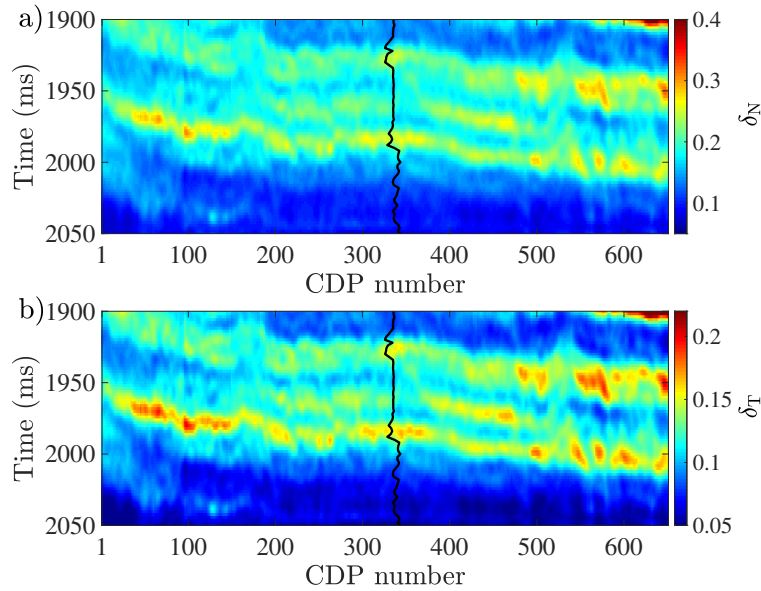
FIG. 13. a) Inversion results of the normal fracture weakness $\delta_{N1}$, and b) Inversion results of the tangential fracture weakness $\delta_{T1}$. The curve is P-wave velocity.

azimuthal angles to implement the estimation of fracture weaknesses using the proposed inversion approach. We conclude that reliable results of fracture weaknesses, which can match the well log and anisotropic AVA gradient, are provided by the inversion approach, which provides the possibility to characterize the fracture connectivity in the hydrocarbon reservoir.

## ACKNOWLEDGMENTS

## APPENDIX A. DERIVATION OF LINEARIZED REFLECTION COEFFICIENTS OF PP AND PS WAVES

Vavryčuk and Pšenčík (1998) proposed an expression of PP-wave reflection coefficient in the case that an interface separates two weakly arbitrary anisotropic media. Extending their PP-wave reflection coefficient to the case that an interface separating isotropic and fractured media, we rewrite the reflection coefficient as

$$
\begin{aligned}
R_{\mathrm{PP}}\left(\theta,\phi\right) \approx & \frac{\Delta\left(C_{33}/\rho\right)}{4\alpha^2}(1+\sin^2\theta) + \left(\frac{1}{2} - 2g\sin^2\theta\right)\frac{\Delta\rho}{\rho} \\
& + \left[\begin{array}{c} \frac{\Delta(C_{13}/\rho+2C_{55}/\rho-C_{33}/\rho)}{2\alpha^2}\cos^2\phi + \frac{\Delta(C_{23}/\rho+2C_{44}/\rho-C_{33}/\rho)}{2\alpha^2}\sin^2\phi \\ -2\frac{\Delta(C_{55}/\rho)}{\alpha^2}\cos^2\phi - 2\frac{\Delta(C_{44}/\rho)}{\alpha^2}\sin^2\phi \end{array}\right]\sin^2\theta \\
& + \left[\begin{array}{c} \frac{\Delta(C_{33}/\rho)}{4\alpha^2} + \frac{\Delta(C_{11}/\rho-C_{33}/\rho)}{4\alpha^2}\cos^4\phi + \frac{\Delta(C_{22}/\rho-C_{33}/\rho)}{4\alpha^2}\sin^4\phi \\ + \frac{\Delta(C_{12}/\rho+2C_{66}/\rho-C_{33}/\rho)}{2\alpha^2}\sin^2\phi\cos^2\phi \end{array}\right]\sin^2\theta\tan^2\theta \\
\approx & \frac{\Delta C_{33}}{4M}(1+\sin^2\theta) + \left(\frac{1}{2} - 2g\sin^2\theta - \frac{C_{33}}{4M} - \frac{C_{33}}{4M}\sin^2\theta\right)\frac{\Delta\rho}{\rho} \\
& + \left[\begin{array}{c} \frac{\Delta(C_{13}+2C_{55}-C_{33})}{2M}\cos^2\phi - \frac{(C_{13}+2C_{55}-C_{33})}{2M}\cos^2\phi\frac{\Delta\rho}{\rho} \\ + \frac{\Delta(C_{23}+2C_{44}-C_{33})}{2M}\sin^2\phi - \frac{(C_{23}+2C_{44}-C_{33})}{2M}\sin^2\phi\frac{\Delta\rho}{\rho} \\ -2\frac{\Delta C_{55}}{M}\cos^2\phi + 2\frac{C_{55}}{M}\cos^2\phi\frac{\Delta\rho}{\rho} \\ -2\frac{\Delta C_{44}}{M}\sin^2\phi + 2\frac{C_{44}}{M}\sin^2\phi\frac{\Delta\rho}{\rho} \end{array}\right]\sin^2\theta \\
& + \left[\begin{array}{c} \frac{\Delta C_{33}}{4M} - \frac{C_{33}}{4M}\frac{\Delta\rho}{\rho} + \frac{\Delta(C_{11}-C_{33})}{4M}\cos^4\phi \\ - \frac{(C_{11}-C_{33})}{4M}\cos^4\phi\frac{\Delta\rho}{\rho} + \frac{\Delta(C_{22}-C_{33})}{4M}\sin^4\phi \\ - \frac{(C_{22}-C_{33})}{4M}\sin^4\phi\frac{\Delta\rho}{\rho} + \frac{\Delta(C_{12}+2C_{66}-C_{33})}{2M}\sin^2\phi\cos^2\phi \\ - \frac{(C_{12}+2C_{66}-C_{33})}{2M}\sin^2\phi\cos^2\phi\frac{\Delta\rho}{\rho} \end{array}\right]\sin^2\theta\tan^2\theta,
\end{aligned}
$$
(A.1)

where $\alpha$ is P-wave velocity of the isotropic background rock, $\theta$ is the angle of incident P-wave, and $\phi$ is azimuthal angle. Substituting equations 4 and 5 into equation A.1, we obtain the expression of PP-wave reflection coefficient after some algebra

$$
\begin{aligned}
R_{\mathrm{PP}}\left(\theta,\phi\right) \approx & \frac{1}{4}\frac{\cos 2\theta}{\cos^2\theta}\frac{\Delta\rho}{\rho} + \frac{1}{4}\sec^2\theta\frac{\Delta M}{M} - 2g\sin^2\theta\frac{\Delta\mu}{\mu} \\
& - \left\{\begin{array}{c} \frac{1}{4}\left[(1-2g)\cos\theta + \cos^2\phi\sin\theta\tan\theta\right]^2 \\ + \frac{(1-2g)}{2}\left[\begin{array}{c}\sec^2\theta - \frac{1}{2}\sin^2\phi\tan^2\theta \\ -g\left(2+\sin^2\phi\tan^2\theta\right)\end{array}\right]\sin^2\theta\sin^2\phi \end{array}\right\}\delta_{N1} \\
& - \left\{\begin{array}{c} \frac{1}{4}\left[(1-2g)\cos\theta + \sin^2\phi\sin\theta\tan\theta\right]^2 \\ + \frac{(1-2g)}{2}\left[\begin{array}{c}\sec^2\theta - \frac{1}{2}\cos^2\phi\tan^2\theta \\ -g\left(2+\cos^2\phi\tan^2\theta\right)\end{array}\right]\sin^2\theta\cos^2\phi \end{array}\right\}\delta_{N2} \\
& + g\cos^2\phi\sin^2\theta\left(1 - \sin^2\phi\tan^2\theta\right)\delta_{T1} \\
& + g\sin^2\phi\sin^2\theta\left(1 - \cos^2\phi\tan^2\theta\right)\delta_{T2}.
\end{aligned}
$$
(A.2)

Shaw and Sen (2006) and Chen et al. (2018) present the relationship between P-to-S reflection coefficient $R_{\mathrm{PS}}$ and scattering potential $\mathcal{S}_{\mathrm{PS}}$ as

$$
\begin{aligned}
R_{\mathrm{PS}} =& \frac{\sin\theta}{2\rho\cos\psi\sin(\theta+\psi)}\mathcal{S}_{\mathrm{PS}} \\
=& \frac{\sin\theta}{2\rho\cos\psi\sin(\theta+\psi)}\left(\Delta\rho\cos 2\theta + \sum_{i=1,j=1}^{i=6,j=6}\Delta C_{ij}\eta_{ij}\right),
\end{aligned}
\tag{A.3}
$$

where $\psi$ is the angle of reflected S-wave. Pertubation in stiffness parameter $\Delta C$ is shown in equation 5, and angle-dependent $\eta$ is expressed as

$$
\begin{aligned}
\eta_{11} =& \frac{\sin^2\theta\sin\psi\cos\psi\cos^4\phi}{\alpha\beta}, \eta_{12} = \frac{\sin^2\theta\sin\psi\cos\psi\sin^2\phi\cos^2\phi}{\alpha\beta}, \\
\eta_{13} =& \frac{\cos^2\theta\sin\psi\cos\psi\cos^2\phi}{\alpha\beta}, \eta_{21} = \eta_{12}, \\
\eta_{22} =& \frac{\sin^2\theta\sin\psi\cos\psi\sin^4\phi}{\alpha\beta}, \eta_{23} = \frac{\cos^2\theta\sin\psi\cos\psi\sin^2\phi}{\alpha\beta}, \\
\eta_{31} =& -\frac{\sin^2\theta\sin\psi\cos\psi\cos^2\phi}{\alpha\beta}, \eta_{32} = -\frac{\sin^2\theta\sin\psi\cos\psi\sin^2\phi}{\alpha\beta}, \\
\eta_{33} =& -\frac{\cos^2\theta\sin\psi\cos\psi}{\alpha\beta}, \eta_{44} = -\frac{\sin 2\theta\cos 2\psi\sin^2\phi}{\alpha\beta}, \\
\eta_{55} =& -\frac{\sin 2\theta\cos 2\psi\cos^2\phi}{\alpha\beta}, \eta_{66} = \frac{2\sin^2\theta\sin 2\psi\sin^2\phi\cos^2\phi}{\alpha\beta},
\end{aligned}
\tag{A.4}
$$

where $\beta$ is S-wave velocity of the isotropic background rock.

Combining equations 5, A.3 and A.4, we obtain the P-to-S reflection coefficient after some algebra

$$
\begin{aligned}
R_{\mathrm{PS}}(\theta,\phi) =& \frac{\sin\theta\cos 2\theta}{2\cos\psi\sin(\theta+\psi)}\frac{\Delta\rho}{\rho} \\
& + \sqrt{g}\frac{\sin\theta(\sin 2\psi+\sin 2\theta\cos 2\psi)}{2\cos\psi\sin(\theta+\psi)}\frac{\Delta\mu}{\mu} \\
& + \frac{1}{\sqrt{g}}\frac{\sin\theta\sin\psi}{\sin(\theta+\psi)}\left[\sin^2\theta\cos^2\phi\left(1-2g^2\right)-g(1-2g)\right]\cos^2\phi\delta_{N1} \\
& - \frac{1}{\sqrt{g}}\frac{\sin\theta\sin\psi}{\sin(\theta+\psi)}\left[2g^2\sin^2\theta\sin^2\phi+g(1-2g)\right]\sin^2\phi\delta_{N2} \\
& + \sqrt{g}\frac{\sin\theta}{2\cos\psi\sin(\theta+\psi)}\left(\sin 2\theta\cos 2\psi-2\sin^2\theta\sin 2\psi\sin^2\phi\right)\cos^2\phi\delta_{T1} \\
& + \sqrt{g}\frac{\sin\theta}{2\cos\psi\sin(\theta+\psi)}\left(\sin 2\theta\cos 2\psi-2\sin^2\theta\sin 2\psi\cos^2\phi\right)\sin^2\phi\delta_{T2}.
\end{aligned}
\tag{A.5}
$$

# REFERENCES

Bakulin, A., Grechka, V., and Tsvankin, I., 2000a, Estimation of fracture parameters from reflection seismic data—Part I: HTI model due to a single fracture set: Geophysics, **65**, No. 6, 1788–1802.

Bakulin, A., Grechka, V., and Tsvankin, I., 2000b, Estimation of fracture parameters from reflection seismic data—Part II: Fractured models with orthorhombic symmetry: Geophysics, **65**, No. 6, 1803–1817.

Chen, H., Zhang, G., Chen, T., and Yin, X., 2018, Joint PP- and PSV-wave amplitudes versus offset and azimuth inversion for fracture compliances in horizontal transversely isotropic media: Geophysical Prospecting, **66**, 561–578.

Chen, H., Zhang, G., Ji, Y., and Yin, X., 2017, Azimuthal seismic amplitude difference inversion for fracture weakness: Pure and Applied Geophysics, **174**, No. 1, 279–291.

Downton, J. E., and Roure, B., 2015, Interpreting azimuthal fourier coefficients for anisotropic and fracture parameters: Interpretation, **3**, No. 3, ST9–ST27.

Guo, J., Rubino, J. G., Glubokovskikh, S., and Gurevich, B., 2018, Dynamic seismic signatures of saturated porous rocks containing two orthogonal sets of fractures: Theory versus numerical simulations: Geophysical Journal International, **213**, No. 2, 1244–1262.

Hunt, L., Reynolds, S., Brown, T., Hadley, S., Downton, J., and Chopra, S., 2010, Quantitative estimate of fracture density variations in the nordegg with azimuthal avo and curvature a case study: The Leading Edge, **29**, No. 9, 1122–1137.

Li, X.-Y., and Crampin, S., 1991, Complex component analysis of shear-wave splitting: theory: Geophysical Journal International, **107**, No. 3, 597–604.

Liu, E., and Martinez, A., 2014, Seismic fracture characterization, vol. 575: Elsevier.

Pšenčík, I., and Gajewski, D., 1998, Polarization, phase velocity, and NMO velocity of qP-waves in arbitrary weakly anisotropic media: Geophysics, **63**, No. 5, 1754–1766.

Pšenčík, I., and Vavryčuk, V., 1998, Weak contrast PP wave displacement R/T coefficients in weakly anisotropic elastic media: pure and applied geophysics, **151**, No. 2-4, 699–718.

Rubino, J., Caspari, E., Müller, T. M., and Holliger, K., 2017, Fracture connectivity can reduce the velocity anisotropy of seismic waves: Geophysical Journal International, **210**, No. 1, 223–227.

Rüger, A., 1998, Variation of p-wave reflectivity with offset and azimuth in anisotropic media: Geophysics, **63**, No. 3, 935–947.

Shaw, R. K., and Sen, M. K., 2006, Use of AVOA data to estimate fluid indicator in a vertically fractured medium: Geophysics, **71**, No. 3, C15–C24.

Vavryčuk, V., and Pšenčík, I., 1998, PP-wave reflection coefficients in weakly anisotropic elastic media: Geophysics, **63**, No. 6, 2129–2141.